Article

Structural Relaxation Enabled by Internal Vacancy Available in a 24-Atom Gold Cluster Reinforces Catalytic Reactivity

Xiao Cai, Weigang Hu, Shun Xu, Dan Yang, Mingyang Chen,* Miao Shu, Rui Si,* Weiping Ding, and Yan Zhu*

Read Online

ACCESS | Metrics & More | Article Recommendations | Supporting Information

ABSTRACT: Unveiling the mystery of the contribution of nonsurface or noninterface sites in a catalyst to its catalytic performance remains a great challenge because of the difficulty in capturing precisely structural information (surface plus inner) encoded in the catalyst. This work attempts to elucidate the critical role of the internal vacancy in an atomically precise 24-atom gold cluster in regulating the catalytic performance on the hydrogenation reaction of CO_2. The experiment results show that the Au_{24} cluster with internal vacancy can mitigate sintering and exhibit high catalytic activity under relatively harsh reaction conditions, in contrast to the structurally similar Au_{25} cluster without internal vacancy. Our computational study suggests that the internal vacancy in Au_{24} provides the cluster with much more structural flexibility, which may be crucial to resisting the aggregation of the cluster and further postponing the deactivation. The hydrogenation and coupling stages of the reaction intermediates are proposed to explain the potential reaction pathway of CO_2 with H_2 on the Au_{24} catalyst with internal vacancy.

$Au_{24}(PPh_3)_{10}(SC_2H_4Ph)_5Cl_2$

Restructuring of Au_{24}

CH_3OCH_3

CO_2 + H_2

● Au ● P ● S ● Cl ⌐ H ● O ● C ○ Vacancy
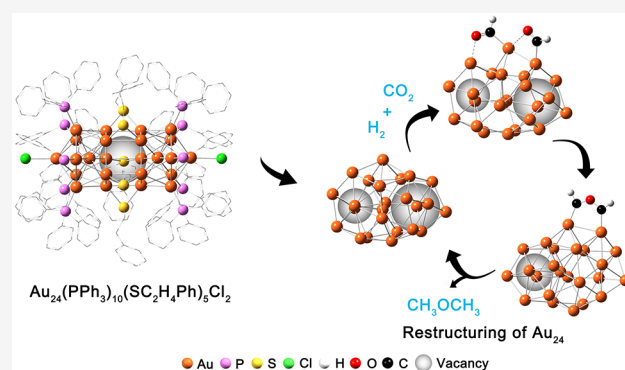
1. INTRODUCTION

The investigations into catalysis of the surface and interface sites of catalysts are always in the research spotlight, considering that the chemical reactions usually occur on the surfaces or interfaces of the catalysts and even a tiny alteration in the surface/interface sites of catalysts can significantly change the catalytic properties.[1−10] An interesting question is whether the inner sites of the heterogeneous catalysts can also have a substantial influence on the catalytic performances. Can one directly observe such an influence in a catalytic reaction? If so, how can the inner and surface sites cooperatively regulate the catalytic process? In recognizing the difficulty in correlating the conventional characterization information with inner sites of a heterogeneous catalyst, a new generation of well-defined catalysts with precise structures is highly desirable. By solving total structures (both the surface and core ones) of such catalysts, one may precisely correlate the catalytic properties with the exact structure of the catalyst and learn what on earth controls the activity, selectivity, and stability of the catalyst.

The emergence of atomically precise metal clusters recently has brought precise synthesis of well-defined catalysts and successful determination of their crystal structures into bloom.[11−18] Based upon the precise structures of these metal clusters, a very fundamental understanding of metal catalysis can be attained at a deep level.[19−22] Among the studies on the catalytic properties of metal clusters, site-specific catalysis of

the clusters has constituted one of the most exciting fields; e.g., it has been found that the central atom of the cluster catalysts can apparently impact the catalytic activity.[23−27] These studies show, in the subnanometer size regime, that the influences of the internal atoms of the cluster catalysts on overall performances should never be ignored. We question naturally whether the internal vacancies as one type of inner sites can possibly contribute to the catalytic performances.

To address this fundamental issue, herein we utilize the atomically precise 24-atom gold cluster with internal vacancy and the 25-atom gold cluster without internal vacancy to investigate how the internal vacancy surrounded by the surface affects the catalytic reactivity of CO_2 hydrogenation, considering that transformation of CO_2 with renewable hydrogenation to yield chemicals and fuels is of significant importance for mitigating global warming and energy supply crises.[28−35] The only structural difference of $[Au_{24}(PPh_3)_{10}(SC_2H_4Ph)_5Cl_2]^+$ (hereafter Au_{24}) and $[Au_{25}(PPh_3)_{10}(SC_2H_4Ph)_5Cl_2]^{2+}$ (hereafter Au_{25}) is that Au_{24} lacks a core gold atom.[36] Au_{24} can be viewed as two vertex-

missing icosahedral Au_{12} units joined by sharing the vacancy, fused together by five thiolate linkages (Figure 1a), whereas

Au_{25} can be viewed as two icosahedral Au_{13} units joined by sharing one vertex gold atom (Figure 1b). The spectroscopic fingerprints of the two clusters allow for an easy identification of the reversible interconversion of the two clusters via one-core-atom removal and addition (Figure S1). Our studies suggest that the internal vacancy in the Au_{24} cluster provides the system with more structural flexibility and the resultant vacancy-protected structural relaxation possibly plays a pivotal role in inhibiting aggregation of the active cluster into inactive nanocrystal, as found for the Au_{25} cluster without the internal vacancy.

Figure 1. X-ray crystal structures of (a) $[Au_{24}(PPh_3)_{10}(SC_2H_4Ph)_5Cl_2]^+$ and (b) $[Au_{25}(PPh_3)_{10}(SC_2H_4Ph)_5Cl_2]^{2+}$ clusters. Color codes: orange = Au, pink = P, yellow = S, green = Cl. H atoms are omitted for clarity.

2. RESULTS AND DISCUSSION

As shown in Figure 2, the Au_{24} and Au_{25} clusters supported on SiO_2 gave rise to similar selectivity toward dimethyl ether (DME) as the major product. Notably, SiO_2 showed no
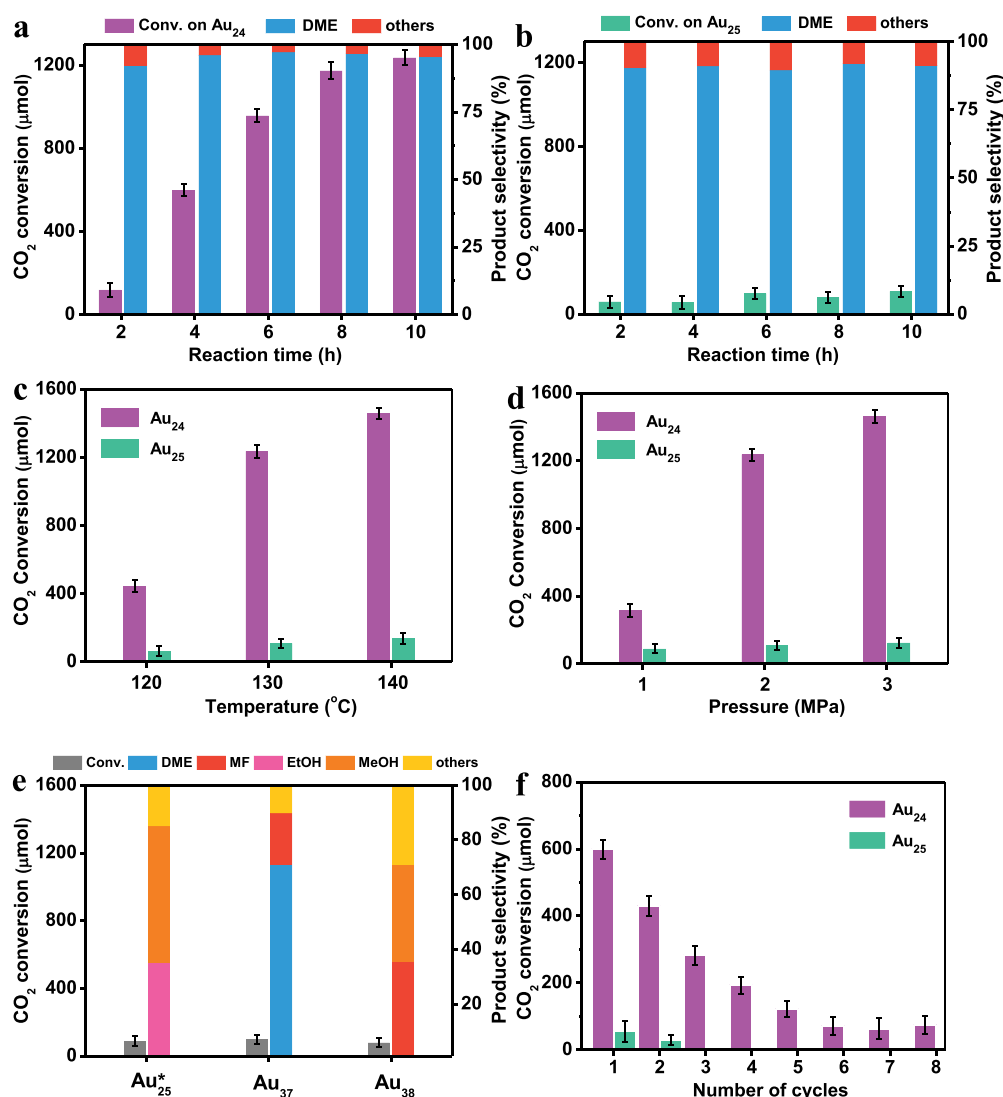
Figure 2. Catalytic performances of CO_2 hydrogenation over (a) Au_{24}/SiO_2 and (b) Au_{25}/SiO_2 catalysts with reaction time. Reaction conditions: 100 mg of $Au_{24/25}/SiO_2$ (0.5% Au), 2 MPa reaction gas ($CO_2:H_2$ = 1:3) with 5% N_2 as an internal standard, 15 mL of H_2O, 130 °C. Note that besides DME other products formed in small amounts were not further studied. (c) Effect of reaction temperature on CO_2 hydrogenation over Au_{24}/SiO_2 and Au_{25}/SiO_2 catalysts with 2 MPa reaction gas for 10 h. (d) Reaction gas pressure-dependent catalytic performances in CO_2 hydrogenation over Au_{24}/SiO_2 and Au_{25}/SiO_2 catalysts at 130 °C for 10 h. (e) Catalytic properties of the supported Au_{25}^*, Au_{37}, and Au_{38} catalysts without internal vacancies for CO_2 hydrogenation with 2 MPa reaction gas at 130 °C for 10 h. Au_{25}^*, $Au_{25}(SC_2H_4Ph)_{18}$; Au_{37}, $[Au_{37}(PPh_3)_{10}(SC_2H_4Ph)_{10}X_2]^+$; Au_{38}, $Au_{38}(SC_2H_4Ph)_{24}$. (f) Recyclability of the Au_{24}/SiO_2 and Au_{25}/SiO_2 catalysts with each 4 h reaction under 2 MPa reaction gas ($CO_2:H_2$ = 1:3) at 130 °C.
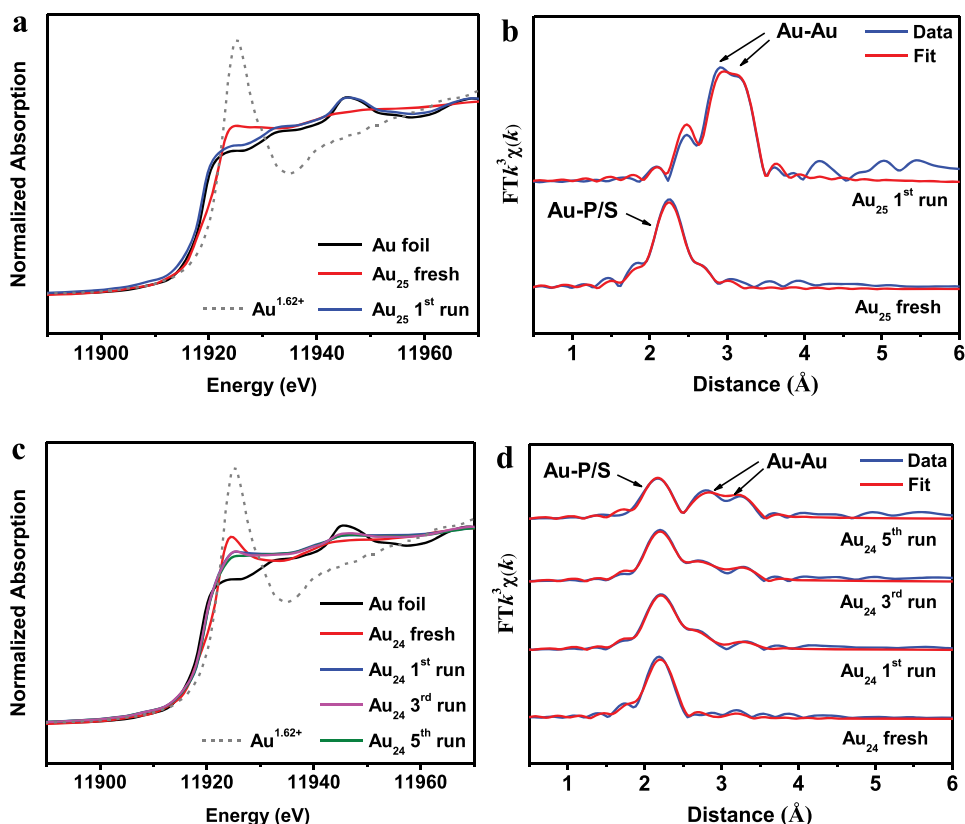
Figure 3. (a) XANES profiles and (b) EXAFS spectra with fits of the Au_{25} catalysts before reaction and after the first run reaction. (c) XANES profiles and (d) EXAFS spectra with fits of the fresh Au_{24} catalyst and the spent Au_{24} catalysts with reaction cycles. The XANES profile of $Au^{1.62+}$ as an oxidic Au standard.[39]

Table 1. Valence of Gold (δ) and EXAFS Fitting Results (R, Distance; CN, Coordination Number; σ^2, Debye−Waller Factor;[a] ΔE_0, Inner Potential Correction[b]) of Au_{24} and Au_{25} with Reaction Cycles

		Au−P/S		Au−Au	
sample	Δ	R (Å)	CN	R (Å)	CN
Au foil	0			2.858 ± 0.002	12
Au_{24} fresh	+0.59	2.32 ± 0.01	2.2 ± 0.2		
		3.02 ± 0.05	0.6 ± 0.3		
Au_{24} first run	+0.35	2.31 ± 0.01	2.1 ± 0.2	2.87 ± 0.02	1.2 ± 0.4
		2.62 ± 0.02	0.9 ± 0.2		
Au_{24} third run	+0.35	2.31 ± 0.01	2.0 ± 0.2	2.88 ± 0.02	2.1 ± 0.4
		2.62 ± 0.02	0.8 ± 0.2		
Au_{24} fifth run	+0.28	2.32 ± 0.01	1.7 ± 0.2	2.86 ± 0.01	3.6 ± 0.4
		2.62 ± 0.05	0.4 ± 0.3		
Au_{25} fresh	+0.31	2.33 ± 0.01	2.5 ± 0.3	2.75 ± 0.06	0.4 ± 0.1
		2.60 ± 0.02	1.0 ± 0.4		
Au_{25} first run	+0.01			2.86 ± 0.01	10.2 ± 0.5

[a]σ^2 = 0.005 and 0.008 Å^2 for all of the analyzed Au−P/S and Au−Au shells, respectively. [b]ΔE_0 varies in the range of 4−9 eV.

activity in the hydrogenation of CO_2 under identical conditions (Figure S2). In addition, neither charge transfer nor surface ligand exchange occurred between gold clusters and SiO_2 (more details shown in Figures S3 and S4). Either CO_2 or H_2 was singly added to the reaction system and no product was detected (Figure S2), which ruled out the participation of the protective ligands of the clusters as carbon sources in forming the organic products. Importantly, a significant difference of the two catalysts was reflected in the catalytic activity. The Au_{24} catalyst can efficiently convert CO_2 to the organic products (Figure 2a), while the Au_{25} catalyst

exhibited quite a low conversion of CO_2 under identical reaction conditions (Figure 2b). The additional experiments at different temperatures and under various reaction gas pressures further showed that the Au_{24} catalyst with internal vacancy exhibited consistently higher catalytic activity than the Au_{25} catalyst without internal vacancy for the hydrogenation reaction of CO_2 (Figure 2c and d). The distinct activities of the Au_{24} and Au_{25} catalysts in the hydrogenation of CO_2 seemed to stem from whether the vacancy is present or absent at the internal sites of the two catalysts.
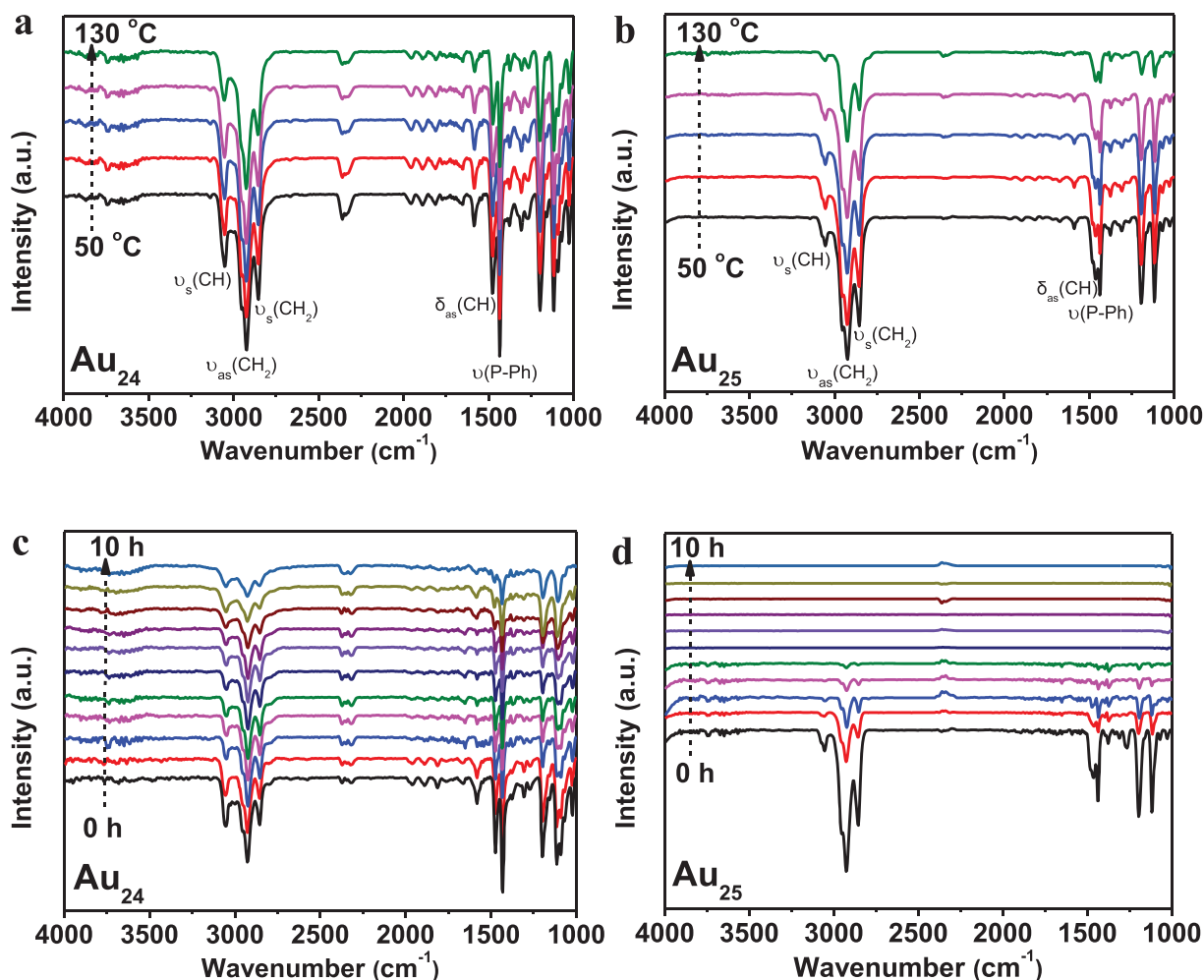
Figure 4. In situ FT-IR spectra of the Au_{24} and Au_{25} clusters under H_2/N_2 (5% H_2) flow: (a, b) at different temperatures; (c, d) at 130 °C for different times.

To further reveal the contribution of the internal vacancy in Au_{24} to the catalytic performance for CO_2 hydrogenation, the three reference clusters with icosahedral Au_{13} kernels, $[Au_{37}(PPh_3)_{10}(SC_2H_4Ph)_{10}X_2]^+$, $Au_{38}(SC_2H_4Ph)_{24}$, and $Au_{25}(SC_2H_4Ph)_{18}$, were performed (Figure 2e). It is worth noting that the three clusters have no internal vacancies: $[Au_{37}(PPh_3)_{10}(SC_2H_4Ph)_{10}X_2]^+$ resembles a rod-like structure assembled from three icosahedral Au_{13} aligned along the rod axis (Figure S5a and b);[37] $Au_{38}(SC_2H_4Ph)_{24}$ can be viewed as a biicosahedral Au_{23} core capped by the remaining 15 gold atoms (Figure S5c and d);[38] $Au_{25}(SC_2H_4Ph)_{18}$ contains a centered icosahedral Au_{13} kernel encapsulated by the remaining 12 gold atoms (Figure S5e and f).[23] Clearly, as shown in Figure 2e, the three reference clusters without internal vacancies exhibited a very low conversion of CO_2. This result again suggested that the Au_{24} catalyst with internal vacancy was more effective than those without internal vacancies for the catalytic hydrogenation of CO_2.

More interestingly, the internal vacancy of Au_{24} could be conducive, to an extent, to mitigating the cluster's aggregation and retaining the cluster's feature. As displayed in Figure 2f, the Au_{25} catalyst lost its catalytic activity after only the first run reaction, due to the severe aggregation of clusters throughout the reaction. X-ray absorption near edge structure (XANES) and extended X-ray absorption fine structure (EXAFS) data

showed that Au_{25} completely degraded into metallic gold after the first run (Figure 3a and b, Table 1). Transmission electron microscopy (TEM) experiments further showed that the Au_{25} clusters after the first run aggregated to form large-sized nanoparticles (nanocrystal) (Figure S6a−c). Note that large Au nanoparticles gave a very low activity under identical reaction conditions. In contrast, deduced from the catalytic recyclability of Au_{24}, the catalytic ability of Au_{24} gradually decreased during the initial six cycles and remained essentially unchanged during the subsequent cycles (Figure 2f). The gradual deactivation of the Au_{24} catalyst was attributed to the fact that the Au_{24} cluster did not substantially grow into the nanocrystal over the reaction cycles. From XANES data (Figure 3c and Table 1), the charge state of the Au_{24} cluster appeared to converge toward an intermediate between the positive valence state of the fresh Au_{24} and the metallic state of Au foil. The presence of the oxidic Au species in the fresh cluster is mainly due to the electron donation from the surface Au atoms to the ligands.[27] From EXAFS analysis (Figure 3d and Table 1), the peaks for the Au−Au bonds intensified and the peaks for the Au−P/Au−S bonds abated over the reaction cycles, implying that a part of the Au_{24} clusters might have been converted into metallic gold clusters during each cycle. Of note, Au−Au bonds in fresh Au_{24} were not observed in EXAFS spectra, due to the thermal fluctuation of Au−Au
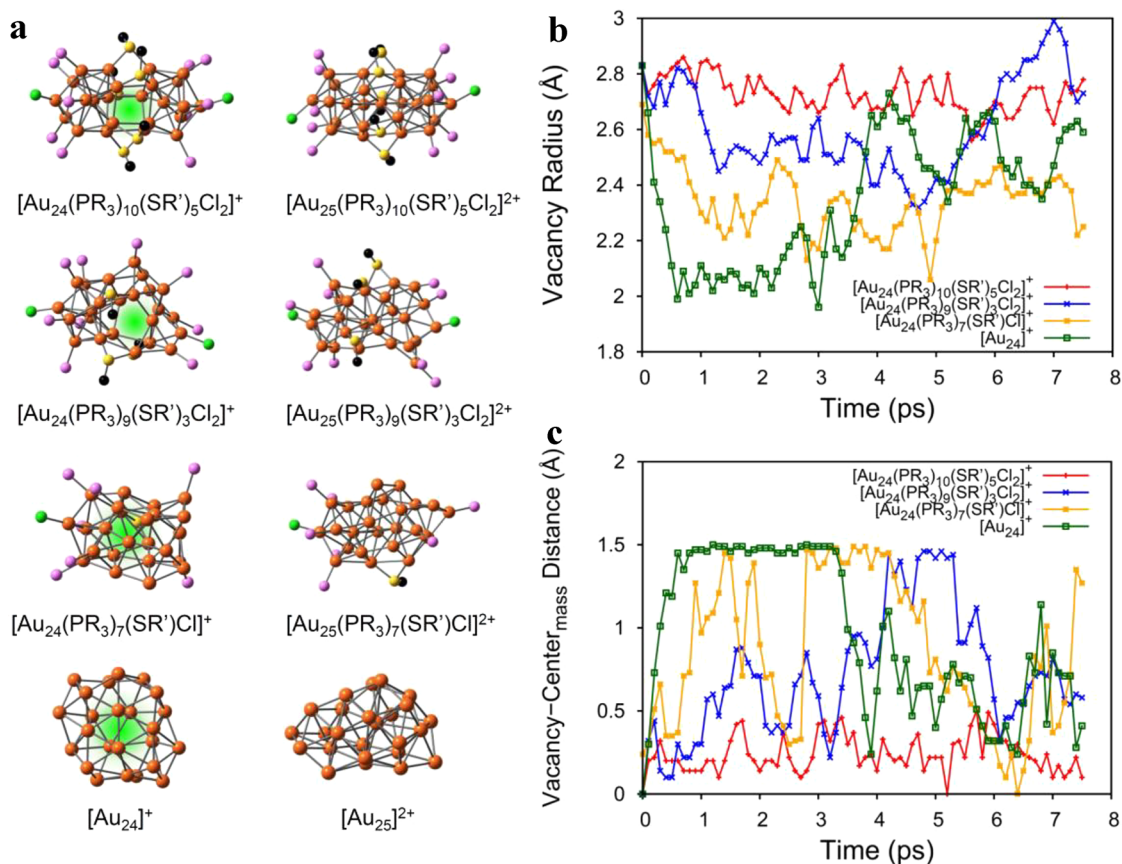
Figure 5. AIMD simulations for the fully passivated, partially depassivated, and fully depassivated Au_{24} and Au_{25} catalysts with an NVT ensemble under a temperature of 400 K. (a) Relaxed cluster structures at 8 ps for Au_{24} and Au_{25} clusters with different degrees of depassivation. (b) Evolution of the vacancy radius in the NVT-AIMD simulations of the fully passivated, partially depassivated, and fully depassivated Au_{24} clusters. (c) The distance between the geometric center of Au atoms and the center of the vacancy as a function of time in the NVT-AIMD simulations of the fully passivated, partially depassivated, and fully depassivated Au_{24} clusters. The atomic vacancies are indicated by light-green spheres. Color codes for elements: orange = Au, pink = P, yellow = S, green = Cl, and black = C. H atoms are omitted. PR_3 (R = H), SR' (R′ = CH_3).

bonds at room temperature.[27,40,41] From Table 1, the coordination number (CN) of Au−Au in Au_{24} increased gradually with cycles (the CN value was 3.6 ± 0.4 for Au_{24} after the fifth reaction), but the coordination number of Au−Au in Au_{25} rose dramatically (the CN value went up to 10.2 ± 0.5 for Au_{25} after the first run, which was close to the CN value of gold foil). In addition, the evolution of the XANES and EXAFS data (Figure S7 and Table S1) of the Au_{24} catalyst with reaction time further confirmed that aggregation of the Au_{24} clusters was much more reluctant under the reaction conditions than that of Au_{25}.

Moreover, the X-ray diffraction (XRD) pattern of fresh Au_{24}/SiO_2 was similar to that of spent Au_{24}/SiO_2, in which the crystal plane of gold was hardly observed in the fresh and spent Au_{24}/SiO_2 (Figure S8a). However, the XRD pattern of fresh Au_{25}/SiO_2 was different from that of spent Au_{25}/SiO_2. As shown in Figure S8b, for the spent Au_{25}/SiO_2 sample, the diffraction peaks at the 2θ of 38.2, 44.5, 64.6, and 77.5°, which were typically indexed as the (111), (200), (220), and (311) diffractions, matching the diffraction pattern of the face-centered cubic (fcc) gold nanocrystal well (JCPDS, PDF No. 03-065-2870). This further indicated that a large-sized gold nanocrystal had been formed from the Au_{25}/SiO_2 reaction system. TEM results also proved that the Au_{24} cluster grew slightly throughout the cycles (Figure S6d−h). The chemical adsorption capability of the Au_{24} and Au_{25} catalysts was probed

by in situ Fourier-transform infrared (FT-IR) spectroscopy. As shown in Figure S9, the intrinsic chemical adsorption capability of Au_{24} dropped with the reaction time of CO_2 hydrogenation, while the chemical adsorption capability of Au_{25} had no longer changes after 2 h reaction, indicating a slow fall in the activity of Au_{24} but a sharp fall in the activity of Au_{25}. These results explicitly revealed the superior stability of the Au_{24} catalyst to the Au_{25} catalyst.

Since the small H_2 molecule was one of the reagents, a fanciful question is whether H_2 could enter the internal vacancy of Au_{24} to protect the structure of Au_{24} during the reaction. To address this, the two clusters were calcinated at 150 °C under H_2/N_2 flow for 1 h, after which the Au_{24} cluster remained robust but the Au_{25} cluster had fully degraded (Figure S10 and Table S2). The result seemed to suggest that the existence of H_2 might maintain the structure of Au_{24}, but the thermal treatment experiment in a vacuum for the cluster ruled out the possibility (Figure S10 and Table S2), as the absence of H_2 did not change the outcomes of the treatment.

Furthermore, the reaction conditions such as the reduction atmosphere and high temperature may not only influence the atom-packing structure of gold atoms but also strongly alter the surface organic ligands. The changes of ligands for the Au_{24} and Au_{25} clusters treated under different conditions were measured by in situ FT-IR spectroscopy. Figure 4a and b showed the IR spectra of the two clusters treated at different

temperatures under the H_2/N_2 flow. The band at 3054 cm^{-1} is assigned to the CH stretching vibration of benzene rings in PPh$_3$ or thiolate ligands.[42] The bands at 2914 and 2851 cm^{-1} are assigned to the asymmetric and symmetric stretching vibrations of CH$_2$ groups in the thiolate, respectively.[43] The band around 1474 cm^{-1} is related to the deformation vibration of CH groups in benzene rings.[44] The band at 1428 cm^{-1} is associated with the stretching vibration of P–Ph in PPh$_3$.[45] As the temperature was increased from 50 to 130 °C, for the Au$_{24}$ cluster, the vibration bands attributed to the CH, CH$_2$, and P–Ph groups in the ligands only declined slightly (Figure 4a). In contrast, for the Au$_{25}$ cluster, the vibration bands associated with the CH, CH$_2$, and P–Ph groups were dramatically weakened with the elevated temperature (Figure 4b). This indicated that a greater amount of ligands including PPh$_3$ and thiolate had been removed from Au$_{25}$, compared to Au$_{24}$. Figure 4c and d showed the change of ligands over time for the two clusters under the treatment of H_2/N_2 and the constant temperature of 130 °C. In particular, the vibration bands associated with the organic ligands in the Au$_{25}$ cluster fully disappeared after a 5 h treatment, whereas those in the Au$_{24}$ cluster remained after a 10 h treatment. The results hinted that the removal of the ligands from the Au$_{24}$ catalyst was comparatively slow, but the exfoliation of ligands from the Au$_{25}$ catalyst was rapid and thorough.

The observation that Au$_{25}$ is prone to aggregation and Au$_{24}$ exhibits good aggregation resistance indicates that Au$_{24}$ is much more catalytically stable than Au$_{25}$ during CO$_2$ hydrogenation. This is opposite from the previous observation on the stability of Au$_{25}$ and Au$_{24}$ in a homogeneous catalytic reaction.[27] The effective physical forms of Au$_{24}$ and Au$_{25}$ in the heterogeneous reaction of CO$_2$ hydrogenation must be totally different from the forms of Au$_{24}$ and Au$_{25}$ in the homogeneous reaction. It is evident from the EXAFS and infrared spectroscopy results that the ligands of Au$_{24}$ and Au$_{25}$ are extensively removed during the CO$_2$ reaction due to comparatively high temperature and hydrogen pressure, suggesting that the Au$_{25}$ and Au$_{24}$ clusters are no longer well passivated. The influences of the depassivation on Au$_{25}$ and Au$_{24}$ were examined using ab initio molecular dynamics (AIMD) simulations with NVT ensembles under the experiment temperature of 400 K for 8 ps (Figure S11 and Figure 5). The structural evolution of the Au$_{24}$ and Au$_{25}$ clusters is found to be dependent on the degree of depassivation. The fully passivated Au$_{24}$ and Au$_{25}$ remain biicosahedral without notable structural reconstruction (Figure 5a). When two thiolates and one phosphide protective ligands are removed from the clusters, the resultant [Au$_{25}$(PR$_3$)$_9$(SR′)$_3$Cl$_2$]$^{2+}$ undergoes small geometry changes with the rod shape essentially retained, and the resultant [Au$_{24}$(PR$_3$)$_9$(SR′)$_3$Cl$_2$]$^+$ exhibits significant geometry changes toward a cage shape with a central vacancy. When four thiolates, three phosphides, and a chloride ligand are removed from the clusters, the resultant [Au$_{25}$(PR$_3$)$_7$(SR′)Cl]$^{2+}$ and [Au$_{24}$(PR$_3$)$_7$(SR′)Cl]$^+$ undergo reconstructions into close-packed and cage-like amorphous clusters, respectively. Such trends in structural evolution extend as the ligands are further removed from the clusters. The fully depassivated [Au$_{25}$]$^{2+}$ reconstructs into a close-packed cluster, and [Au$_{24}$]$^+$ becomes a cage with an interior vacancy. Our AIMD simulation results suggest that maintaining the biicosahedral shapes of Au$_{24}$ and Au$_{25}$ requires essentially full passivation. Depassivated Au$_{25}$ reconstructs into the close-packed cluster without any interior vacancy which, despite being amorphous,

is structurally akin to the fcc crystal. Depassivated Au$_{24}$ reconstructs into the cage-shaped cluster. The vacancy originating from the biicosahedral [Au$_{24}$(PR$_3$)$_{10}$(SR′)$_5$Cl$_2$]$^+$ is preserved during the reconstructions for all degrees of depassivation (Figure 5b). Interestingly, the vacancies of the depassivated Au$_{24}$ clusters are animate during the structural evolution, in terms of both structure and location, as indicated by the drifting of the vacancy in the reconstructing cluster (Figure 5c). In other words, the vacancy is not annihilated despite that the depassivated Au$_{24}$ cluster undergoes dynamic structure reconstruction.

We have shown that whether there exists a vacancy in the Au cluster leads to different reconstruction behaviors following the depassivation. Is the depassivation thermally viable, will the reconstructing depassivated clusters aggregate, and what role can the vacancy potentially play during the aggregation? To answer these questions, the thermodynamics for the depassivation of [Au$_{25}$(PPh$_3$)$_{10}$(SC$_2$H$_4$Ph)$_5$Cl$_2$]$^{2+}$ and [Au$_{24}$(PPh$_3$)$_{10}$(SC$_2$H$_4$Ph)$_5$Cl$_2$]$^+$ and the initial aggregation of the depassivated clusters were predicted at the density functional theory (DFT) level. The dissociation of the PPh$_3$ phosphine is calculated to be endothermic by ∼180 kJ/mol, and the removals of the SC$_2$H$_4$Ph thiolate and chloride ligands are predicted to be less than 90 kJ/mol for both clusters (Figure S12), indicating facile removal of ligands at high temperature in the presence of H$_2$. Thus, the Au$_{25}$ and Au$_{24}$ clusters during the CO$_2$ hydrogenation might be fully or partially depassivated. Here we consider the extreme situation where [Au$_{25}$(PPh$_3$)$_{10}$(SC$_2$H$_4$Ph)$_5$Cl$_2$]$^{2+}$ and [Au$_{24}$(PPh$_3$)$_{10}$(SC$_2$H$_4$Ph)$_5$Cl$_2$]$^+$ are fully depassivated to form [Au$_{25}$]$^{2+}$ and [Au$_{24}$]$^+$. Direct DFT optimization calculations and AIMD simulations lead to different structures for the fully depassivated clusters. From direct DFT optimization calculations, the fully depassivated [Au$_{25}$]$^{2+}$ remains the biicosahedron, whereas [Au$_{24}$]$^+$ undergoes a spontaneous relaxation to form a double-cage structure that contains a small vacancy and a large vacancy (Figure S13). The AIMD simulations find [Au$_{25}$]$^{2+}$ as a close-packed amorphous cluster and [Au$_{24}$]$^+$ as a single-walled cage, which are 284 and 14 kJ/mol more stable than the biicosahedron [Au$_{25}$]$^{2+}$ and the double-cage [Au$_{24}$]$^+$, respectively (Figure S13). Note that the double-cage [Au$_{24}$]$^+$ not only is nearly as stable as the single-walled cage [Au$_{24}$]$^+$ but also structurally resembles the partially depassivated Au$_{24}$ clusters from AIMD ([Au$_{24}$(PR$_3$)$_7$(SR′)Cl]$^+$ and [Au$_{24}$(PR$_3$)$_9$(SR′)$_3$Cl$_2$]$^+$) to some extent. The double-cage [Au$_{24}$]$^+$ and close-packed [Au$_{25}$]$^{2+}$ are considered to represent the depassivated Au$_{24}$ and Au$_{25}$ clusters during the CO$_2$ hydrogenation, respectively, and are used in further computations. As shown in Figure S14, the total energy for the full depassivation of the Au$_{25}$ catalyst that leads to the close-packed [Au$_{25}$]$^{2+}$ is calculated to be 1805 kJ/mol with $^7/_2$ equiv of H$_2$ involved, and the total depassivation energy for the double-cage [Au$_{24}$]$^+$ is 1521 kJ/mol. The much lower depassivation energy of [Au$_{24}$]$^+$ suggests that [Au$_{24}$]$^+$ has a much lower surface energy than [Au$_{25}$]$^{2+}$.

The initial aggregation of the [Au$_{25}$]$^{2+}$ and [Au$_{24}$]$^+$ clusters can be achieved by atomic gold migration, i.e., gold atoms being transferred from one cluster to another to form larger clusters, analogous to Ostwald ripening. According to DFT results (Figure S14), both [Au$_{25}$]$^{2+}$ and [Au$_{24}$]$^+$ exhibit Au dissociation energy comparable to Au affinity, and the 2[Au$_{25}$]$^{2+}$ → [Au$_{24}$]$^{2+}$ + [Au$_{26}$]$^{2+}$ and 2[Au$_{24}$]$^+$ → [Au$_{23}$]$^+$ + [Au$_{25}$]$^+$ migration reactions are both mildly exothermic (ΔH =
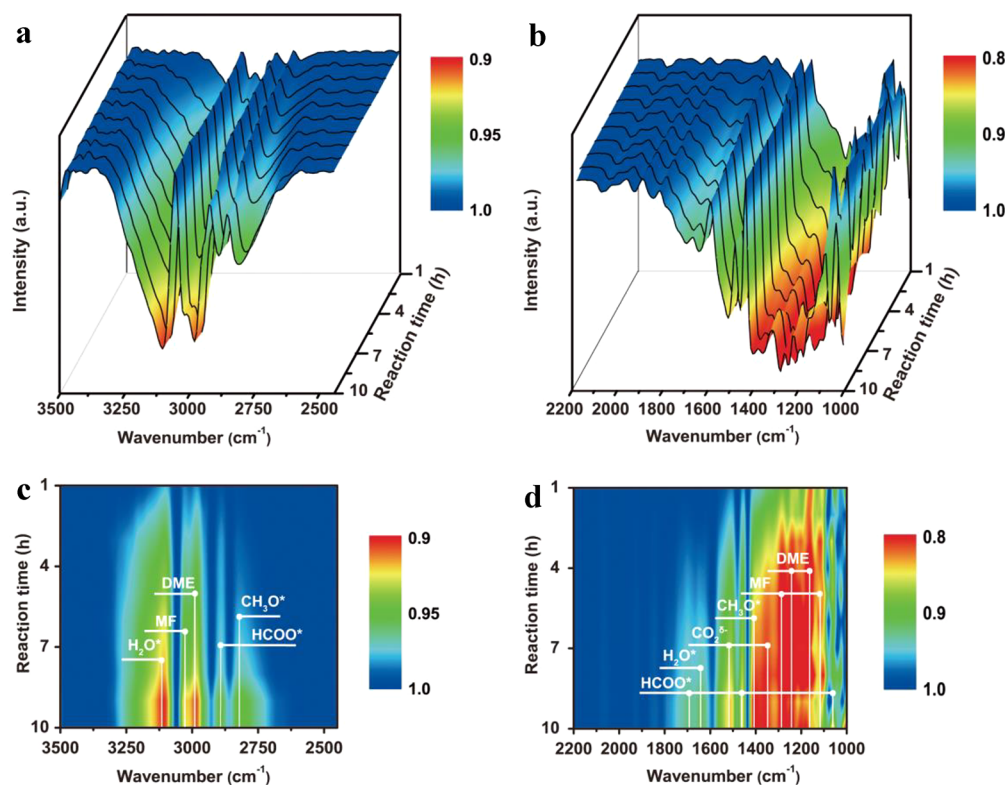
Figure 6. Time-resolved in situ FT-IR results of surface species formed on the Au_{24} catalyst with 2 bar of reaction gas (CO_2:H_2 = 1:3): (a) in situ FT-IR spectra from 3500 to 2450 cm^{-1}; (b) in situ FT-IR spectra from 2200 to 1000 cm^{-1}; (c) contour map from 3500 to 2450 cm^{-1}; (d) contour map from 2200 to 1000 cm^{-1}.
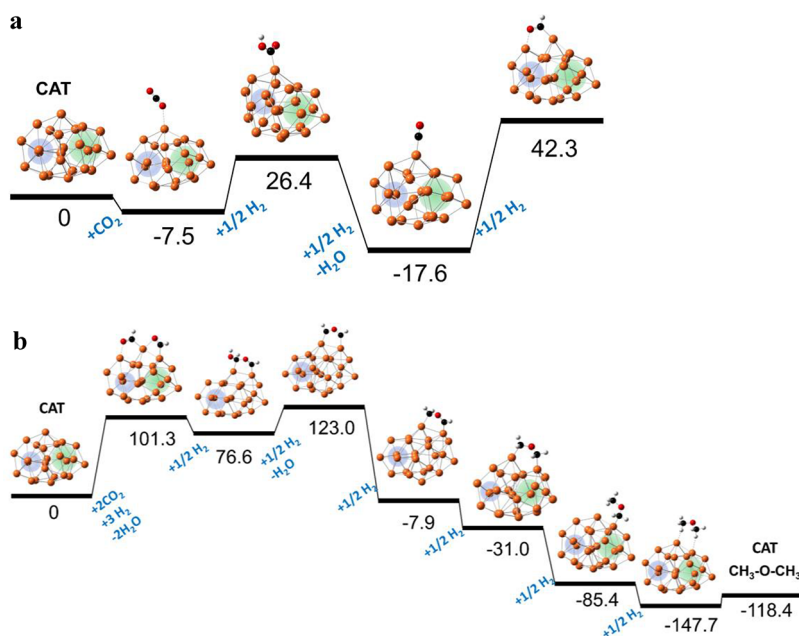
Figure 7. Calculated potential energy surfaces for CO_2 hydrogenation to form DME at the DFT level with PBE/Aug-cc-pVDZ(-pp): (a) RWGS to form one-site Au−CHO intermediate species and (b) two-site coupling reaction to form DME. Color codes for elements: orange = Au, pink = P, yellow = S, green = Cl, black = C, red = O, and white = H. CAT = catalyst. Blue and green spheres indicate the small and large vacancies in the catalyst. Reaction enthalpies at 0 K are given in kJ/mol.

−10 and −17 kJ/mol, respectively). Therefore, the initial aggregation is spontaneous for both fully depassivated clusters. Both the optimized $[Au_{23}]^+$ and $[Au_{25}]^+$ contain an interior vacancy (Figure S14). It is therefore hypothesized that the vacancy of $[Au_{24}]^+$ may be preserved during the initial

aggregation and is likely to be persistent throughout the aggregation. We hypothesize that the different aggregation behaviors of the depassivated Au_{24} and Au_{25} clusters are governed by the presence/absence of the interior vacancy. Previous computational and experimental studies suggested an

intrinsic size−structure relationship for Au_n (where n is the gold atom number) clusters, where amorphous and cage structures[46−52] dominate small cluster sizes $n < 30$ while the fcc-crystal structure motif[53,54] prevails for $n = 20$ and $n > 35$. The sizes of the Au_{24} and Au_{25} clusters are only slightly below the critical size for the amorphous-to-fcc transition. Hence, the close-packed amorphous $[Au_{25}]^{2+}$ is expected to grow into the fcc cluster facilely. For growth of $[Au_{24}]^+$ beyond the critical size, the persistent vacancies might divide the particle into regions containing de facto small amorphous Au clusters that locally follow the intrinsic size−structure relationship of gold particles, and the whole cluster might remain amorphous. This could be why the Au_{25} catalysts spontaneous grow into large fcc nanoparticles under experimental conditions while the Au_{24} catalysts exhibit much lower aggregation propensity and are not fully grown into fcc nanoparticles, as found by the experiment.

We next turned our attention to the potential reaction mechanism of CO_2 hydrogenation on the Au_{24} catalyst. In situ monitoring of the reaction intermediates formed on the two catalysts was performed by time-resolved in situ FT-IR spectroscopy during the interaction of the catalysts with 2 bar of reaction gas (CO_2:H_2 = 1:3) at 130 °C. For the Au_{24} reaction system, as shown in Figure 6, the bands at 2954, 2824, and 1404 cm^{-1} are assigned to the asymmetric and symmetric C−H stretches of methoxy groups and C−H bending vibrations, respectively.[55] The bands at 2892, 1696, 1457, and 1065 cm^{-1} are associated with formate species, in which the first three bands arise from the C−H, C=O, and C−O stretching modes of formate groups[56,57] and the last band is attributed to the C−H scissoring vibration of formate groups.[58] The stretching vibrations of C−O−C of DME were found at 1249 and 1180 cm^{-1}, and the asymmetric C−H stretching vibration of DME appeared at 2992 cm^{-1}.[59−61] The other three IR bands observed at 3031, 1280, and 1140 cm^{-1} are respectively assigned to the CH_3 rocking, C−O stretching, and C−H stretching vibrations of methyl formate (MF).[62] In addition, the absorption bands close to 3108 and 1642 cm^{-1} correspond to the O−H stretching and in-plane deformation vibrations of interfacial water, respectively.[63] The IR band at 2075 cm^{-1} is assigned to CO adsorbed on Au sites.[64] The characteristic peaks of the carboxylate ($CO_2^{\delta-}$) species were located near 1515 and 1357 cm^{-1}.[57,58] For the Au_{25} reaction system, the IR signals of the formate, methoxy, and DME species were also detected (Figure S15). Noticeably, the intensities of these IR bands for the Au_{25} catalyst were much lower than those for the Au_{24} catalyst, implying the higher reactivity of Au_{24} than Au_{25} in CO_2 activation and hydrogenation.

Going further, the calculated potential energy surface (PES) for the CO_2 hydrogenation leading to the DME major product over the fully depassivated double-cage Au_{24}^+ derived from $[Au_{24}(PPh_3)_{10}(SC_2H_4Ph)_5Cl_2]^+$ is shown in Figure 7. A two-stage reaction mechanism is proposed, comprising a one-carbon (C_1) hydrogenation stage and a two-carbon (C_2) coupling stage. During the first stage, the one-carbon (C_1) hydrogenation occurs first to form Au(CHO) at an exposed Au following the reverse water−gas shift (RWGS) reaction path (Figure 7a), similar to the CO_2 hydrogenation catalyzed by Cu/ZnO catalysts.[65] The reaction path is briefly described as $CO_2 \rightarrow Au(COOH) \rightarrow Au(CO) \rightarrow Au(CHO)$. In Au(CHO), O forms an additional bond with the Au adjacent to the C−Au. It is noted that the vacancies in Au_{24}^+ are well preserved during

the C_1 hydrogenation stage. The second stage occurs when a second CO_2 attacks a Au site that is adjacent to the existing Au(CHO) site, which results in a (CHO)Au(CHO) intermediate with two C_1 ligands (Figure 7b). In (CHO)Au-(CHO), the adsorption of the two CHO ligands is asymmetric, and Au is bonded to C and O atoms from the two ligands separately. It should be pointed out that the atomic vacancies remain in Au_{24}^+ upon the formation of (CHO)Au(CHO). The two CHO ligands of the (CHO)Au(CHO) species can undergo a C−O coupling reaction with $^1/_2$ equiv of H_2 and spontaneously form a C_2 η^2 HO−CH−O−CH ligand bridging the two adjacent exposed Au atoms ($\Delta H = -25$ kJ/mol) due to the asymmetric dual-ligand adsorption. Notably, the Au_{24}^+ double-cage is squeezed upon the formation of HO−CH−O−CH and a vacancy in Au_{24}^+ disappears consequently. Such relaxation of the Au_{24}^+ double-cage should release the stress between the two Au sites caused by the strong η^2 adsorption and stabilize the HO−CH−O−CH intermediate, and hence favors the coupling reaction. Further hydrogenation of HO−CH−O−CH leads to HC−O−CH and H_2C−O−CH η^2 C_2 intermediates, with the vacancy remaining disappeared from Au_{24}^+. Upon the formation of the subsequent hydrogenation intermediates and product, i.e., H_2C−O−CH_2, H_3C−O−CH_2, and DME, the missing vacancy grows back (Figure 7b) as the Au_{24}^+ catalyst is blown up to return to the unreacted state. This suggests that the deformation of the double-cage is reversible and the vacancy can be regenerated within the catalytic cycle when the bridge adsorption is weakened (as for H_2C−O−CH_2) or destroyed (as for H_3C−O−CH_2). The formation mechanism of DME on the 24-atom gold catalyst provides a new insight that is different from the conventional two-step mechanism comprising methanol synthesis via hydrogenation of CO_2 and methanol dehydration to form DME.[66]

Note that, in the DFT calculations, the fully depassivated Au_{24}^+ is chosen to understand the aggregation and catalytic mechanism during the CO_2 hydrogenation. From the experimental results, we are aware that the depassivation of $[Au_{24}(PPh_3)_{10}(SC_2H_4Ph)_5Cl_2]^+$ is slower than that of $[Au_{25}(PPh_3)_{10}(SC_2H_4Ph)_5Cl_2]^{2+}$, and some protective ligands remain on the Au_{24} clusters during the reaction. The fully depassivated Au_{24}^+ is chosen because: (1) the infrared and EXAFS data give average characteristics of the reaction system, which does not rule out the existence of Au_{24}^+; (2) the partially depassivated Au_{24} clusters as intermediate states are expected to contain vacancies, since the two extreme states ($[Au_{24}(PPh_3)_{10}(SC_2H_4Ph)_5Cl_2]^+$ and Au_{24}^+) contain vacancies; (3) the realistic Au_{24} clusters, which could be partially depassivated and slightly aggregated, are likely to contain local structures represented by Au_{24}^+, which is supported by the AIMD results. Overall, on the basis of DFT calculations and theory, it is suggested that the depassivated and aggregated $[Au_{24}(PPh_3)_{10}(SC_2H_4Ph)_5Cl_2]^+$ could contain non-fcc cage-like subsurface local structures, which may exhibit breath-like motions to promote the coupling of reaction intermediates with decent catalytic recyclability.

3. CONCLUSIONS

To summarize, we report the potential contribution of the internal vacancy/cage in the Au_{24} catalyst to the catalytic performance on the CO_2 hydrogenation. The experimental studies show that the Au_{24} cluster with internal vacancy is much more reluctant to aggregate into a large-size nanocrystal and further exhibits enhanced activity and stability, compared

to the Au_{25} cluster without internal vacancy. DFT computations and theory suggest that not only the vacancy of Au_{24} is possibly preserved during the reaction at different surface ligand coverages, but also vacancy-protected structural relaxation may mitigate the sintering and deactivation of the Au_{24} catalyst. In addition, we propose a molecular-level two-stage reaction pathway of CO_2 hydrogenation on the Au_{24} catalyst toward DME product. We anticipate that the exploration of potential influences of internal vacancies on catalytic properties can bring a new scientific vision in understanding the contributions of nonsurface/noninterface sites on the overall catalytic performances.

4. EXPERIMENTAL AND COMPUTATIONAL METHODS

4.1. Catalyst Synthesis. $[Au_{24}(PPh_3)_{10}(SC_2H_4Ph)_5Cl_2]^+$ and $[Au_{25}(PPh_3)_{10}(SC_2H_4Ph)_5Cl_2]^{2+}$ clusters were synthesized using the previous procedures.[36] A 0.2 mmol portion of $HAuCl_4·4H_2O$ in 5 mL of pure H_2O was added to 10 mL of toluene. After 20 min, the aqueous phase was removed by a glass tube. A 0.6 mmol portion of PPh_3 was added to the toluene phase after 0.6 mmol of $NaBH_4$ dissolved in 6 mL of ethanol was poured. After 2 h, the solution was evaporated to obtain the black crude product, and 15 mL of dichloromethane was applied to extract the precursor. A 200 μL portion of PhC_2H_4SH was added to the above dichloromethane solution of black product. The solution was kept at 40 °C for 12 h. The Au_{25} was purified with hexane and extracted with ethanol. Then, 20 mg of purified Au_{25} clusters and 1.2 g of PPh_3 were mixed in 10 mL of dichloromethane. The reaction continued for 24 h at 40 °C. The Au_{24} clusters were obtained after being washed with hexane and extracted with toluene.

$[Au_{37}(PPh_3)_{10}(SC_2H_4Ph)_{10}X_2]^+$ was synthesized as follows.[37] A 0.2 mmol portion of $HAuCl_4·4H_2O$ in 5 mL of pure H_2O was mixed with 0.233 mmol of tetra-n-octylammonium bromide (TOAB) in 10 mL of toluene. After 20 min, the aqueous phase was removed by a glass tube. A 0.6 mmol portion of PPh_3 was added to the toluene solution, after 0.6 mmol of $NaBH_4$ dissolved in 6 mL of ice-cold water was poured. After 2 h, the solution was evaporated to obtain the crude product and 15 mL of dichloromethane was applied to extract the precursor. A 200 μL portion of PhC_2H_4SH was added to the above solution. The solution was kept at room temperature for 36 h. The product was purified with methanol and extracted with acetonitrile/DCM (3:1).

$Au_{38}(SC_2H_4Ph)_{24}$ was synthesized based on the reported method.[38] A 0.5 mmol portion of $HAuCl_4·4H_2O$ and 2.0 mmol of glutathione were dissolved in 20 mL of acetone under vigorous stirring for 30 min. The mixture was then cooled to 0 °C. After 30 min, a solution of $NaBH_4$ (5 mmol, dissolved in 6 mL of cold water) was rapidly added. After 30 min, 6 mL of water was added to dissolve the precipitations. Then, the solution was mixed with 0.3 mL of ethanol, 2 mL of toluene, and 2 mL of PhC_2H_4SH. The solution was kept at 80 °C for 40 h. The organic phase was washed with ethanol to remove excess thiol. The product was extracted with toluene.

$Au_{25}(SC_2H_4Ph)_{18}$ was synthesized based on the reported method.[23] A 0.203 mmol portion of $HAuCl_4·3H_2O$ and 0.235 mmol of TOAB were added to 15 mL of THF. After stirring for 30 min, 0.140 mL of phenylethanethiol was added to the above mixture. After 1 h, $NaBH_4$ (76.8 mg, dissolved in 5 mL of cold water) was added to the mixture at once. The reaction was stopped after 3 h. The crude product solution was dried by a rotary evaporator and washed with methanol and then collected by centrifugation.

Preparation of Au_n/SiO_2. The supported Au_n catalysts were obtained by stirring a solution of Au_n clusters in dichloromethane with a calculated amount of SiO_2 (fumed, 140 m^2/g) for 12 h, and the solution was removed in flowing nitrogen. The loading weight of gold was detected by ICP (inductively coupled plasma–atomic emission spectroscopy).

4.2. CO_2 Hydrogenation. A 100 mg portion of catalyst (~0.5% Au clusters) was added into a stainless-steel autoclave equipped with

an automatic temperature control system, and the magnetically driven impeller was used to disperse catalyst in 15 mL of pure water. The temperature was heated to 130 °C, and the vessel was then pressurized by 2 MPa of mixed gas of CO_2 and H_2 with 5% N_2 as an internal standard under stirring of 800 rpm. The ratio of CO_2 and H_2 is 1:3. After a certain amount of time, the reaction was stopped. The catalytic products were analyzed by GC9860 equipped with a thermal conductivity detector with a TDX-1 column and a flame ionization detector with an FFAP and PLOT-Q capillary column.

The Cycle Experiments. The mixture after reaction was centrifuged to isolate the catalyst, and then, the catalyst was washed with pure water several times. After that, the catalyst was reintroduced into the reactor to start a new run of reaction. The data presented in Figure 2f are the new performance of the reused catalyst in every 4 h run.

4.3. Characterization. UV–vis absorption spectra were recorded using a SHIMADZU UV-1800 with a medium sampling scan rate. Transmission electron microscopy (TEM) was recorded with a JEM-200CX (JEOL, Japan) at a 100 kV acceleration voltage. The loading weight of Au was determined via inductively coupled plasma–atomic emission spectroscopy (ICP-AES, Optima 5300DV). The binding energies of the surface species on the catalysts were determined by X-ray photoelectron spectroscopy (XPS) (Thermo Scientific K-Alpha) using Al Kα ($h\nu$ = 1486.6 eV) as the excitation source. Powder X-ray diffraction (XRD) patterns of the samples were recorded on a Bruker D8 ADVANCE X.

The X-ray absorption fine structure (XAFS) spectra at the Au L_3 (E_0 = 11919.0 eV) edge were performed at the BL14W1 beamline[67] of Shanghai Synchrotron Radiation Facility (SSRF) operated at 3.5 GeV under "top-up" mode with a constant current of 240 mA. The XAFS data were recorded under fluorescence mode with a Lytle ion chamber at room temperature. The energy was calibrated according to the absorption edge of pure Au foil. Athena and Artemis codes were used to extract the data and fit the profiles. The XAFS data of the fresh Au_{24}/Au_{25} samples were from the previous report.[27] For the X-ray absorption near edge structure (XANES) part, the experimental absorption coefficients as function of energies $\mu(E)$ were processed by background subtraction and normalization procedures and reported as "normalized absorption" with E_0 = 11919.0 eV for all of the samples and Au foil standard. Based on the normalized XANES profiles, the average valence of gold can be determined by the white-line intensity with the help of the above standard references. For the extended X-ray absorption fine structure (EXAFS) part, the Fourier-transform (FT) data in R space were analyzed by applying first shell approximation and metallic Au models for Au–P/Au–S and Au–Au contributions, respectively. The passive electron factors were determined by fitting the experimental data on Au foil and fixing the coordination number (CN) of Au–Au to be 12 and then fixing for further analysis of the measured samples. The parameters describing the electronic properties (e.g., correction to the photoelectron energy origin, ΔE_0) and local structure environment including CN, bond distance (R), and Debye–Waller factor around the absorbing atoms (σ^2) were allowed to vary during the fit process. The fitted ranges for k and R spaces were selected to be k = 3–13 Å^{-1} with R = 1.0–3.0 Å (k^3 weighted).

Time-resolved in situ FT-IR experiments were carried out in an elevated pressure cell with a TENSOR 27 (Sample Compartment LN-MCT Mid). To understand the reaction mechanism, the temperature was raised from room temperature to 130 °C at 4 °C/min while purging with Ar flow and then the background spectrum of the catalyst was acquired. Then, the elevated pressure cell was pressurized by 2 bar of mixed gas (CO_2:H_2 = 1:3) for different periods of time and then measured by in situ FT-IR.

In situ IR spectra of CO adsorption were collected using TENSOR 27 (Sample Compartment RT-DLaTGS). IR spectra were recorded continuously to study the surface changes. In order to follow surface changes over reaction time, the elevated pressure cell was pressurized by 2 bar of mixed gas (CO_2:H_2 = 1:3) at 130 °C for different periods before spectra collection. Then, after flowing 1 bar of Ar for 0.5 h at 150 °C, the sample was then cooled to room temperature and the background spectrum was collected in Ar flow. CO adsorption was conducted at room temperature for 30 min, and Ar flow was switched

back to purge gaseous CO. IR spectra of CO adsorbed onto the samples were recorded.

In situ IR spectra of the Au_{24} and Au_{25} clusters under H_2/N_2 flow at different temperatures or at 130 °C for different times were collected using TENSOR 27 (Sample Compartment RT-DLaTGS). KBr under H_2/N_2 flow was scanned as a background spectrum, and Au_{24} and Au_{25} dichloromethane solution was respectively dropped on KBr and then heated under an infrared lamp to remove the solvent. The temperature was raised to 130 °C at 4 °C/min under H_2/N_2 flow, and IR spectra were recorded at a specific temperature. Or the temperature was kept at 130 °C and IR spectra were collected at a specific time. In situ IR spectra of the Au_{24}/SiO_2, Au_{25}/SiO_2, and SiO_2 samples under H_2/N_2 (5% H_2) or Ar flow at 130 °C were collected using TENSOR 27. KBr was heated under H_2/N_2 or Ar flow at 130 °C and scanned as a background spectrum. Each sample was mixed with KBr and then placed into the cell after compress. The temperature was raised to 130 °C at 4 °C/min under H_2/N_2 or Ar flow, and then, the IR spectra were collected at an interval of 2 min.

4.4. Computational Methods. The CO_2 hydrogenation reaction catalyzed by the heterogeneous Au_{24} and Au_{25} catalysts was modeled using the density functional theory[68] (DFT) level with the PBE functional.[69] Local geometry optimization and vibrational frequency calculations were carried out for the important catalytic species during the hydrogenation catalysis using the Gaussian 09 software package.[70]

Ab initio molecular dynamics (AIMD)[71] simulations were used to model the reconstruction of Au_{24} and Au_{25} catalysts with different degrees of depassivation (i.e., removal of protective ligands). Four sets of AIMD simulations were performed: (1) intact $[Au_{24}(PH_3)_{10}(SCH_3)_5Cl_2]^+$ and $[Au_{25}(PH_3)_{10}(SCH_3)_5Cl_2]^{2+}$ catalysts, (2) catalysts with 2 SCH_3 and 1 PH_3 removed, (3) catalysts with 4 SCH_3, 2 PH_3, and 1 Cl removed, and (4) fully depassivated metallic catalysts. The AIMD simulations were performed with an NVT ensemble (attached to a Nosé–Hoover thermostat[72,73]) at 400 K (or 130 °C). The calculations employed the Gaussian and plane wave method (GPW)[74] implemented in the CP2K software package[75] at the DFT level of theory with the PBE exchange-correlation functional and a DZVP-MOLOPT-SR-GTH[76] basis set and pseudopotential.

The fully passivated (fresh) Au_{24} and Au_{25} clusters were modeled with simplified $[Au_{24}(PH_3)_{10}(SCH_3)_5Cl_2]^+$ and $[Au_{25}(PH_3)_{10}(SCH_3)_5Cl_2]^{2+}$ models at the PBE level with the Aug-cc-pVDZ(-pp) basis set and pseudopotential,[77–79] where the PPh_3 ligands of the catalysts were replaced by PH_3 and the SCH_2CH_2Ph ligands were replaced by SCH_3. The zero-point energy corrections were considered for all of the relative species and were included in the reaction enthalpies.

The depassivation of the $[Au_{24}(PH_3)_{10}(SCH_3)_5Cl_2]^+$ and $[Au_{25}(PH_3)_{10}(SCH_3)_5Cl_2]^{2+}$ was tested for each ligand, as given by eqs 1–6:

$$[Au_{24}(PH_3)_{10}(SCH_3)_5Cl_2]^+ \rightarrow [Au_{24}(PH_3)_9(SCH_3)_5Cl_2]^+ + PH_3 \tag{1}$$

$$[Au_{24}(PH_3)_{10}(SCH_3)_5Cl_2]^+ + H_2$$
$$\rightarrow [Au_{24}(PH_3)_{10}(SCH_3)_4HCl_2]^+ + HSCH_3 \tag{2}$$

$$[Au_{24}(PH_3)_{10}(SCH_3)_5Cl_2]^+ + H_2$$
$$\rightarrow [Au_{24}(PH_3)_{10}(SCH_3)_5HCl]^+ + HCl \tag{3}$$

$$[Au_{25}(PH_3)_{10}(SCH_3)_5Cl_2]^{2+}$$
$$\rightarrow [Au_{25}(PH_3)_9(SCH_3)_5Cl_2]^{2+} + PH_3 \tag{4}$$

$$[Au_{25}(PH_3)_{10}(SCH_3)_5Cl_2]^{2+} + H_2$$
$$\rightarrow [Au_{25}(PH_3)_{10}(SCH_3)_4HCl_2]^{2+} + HSCH_3 \tag{5}$$

$$[Au_{25}(PH_3)_{10}(SCH_3)_5Cl_2]^{2+} + H_2$$
$$\rightarrow [Au_{25}(PH_3)_{10}(SCH_3)_5HCl]^{2+} + HCl \tag{6}$$
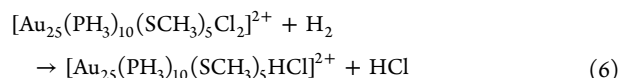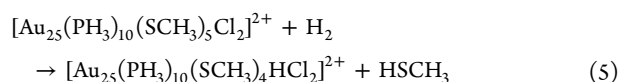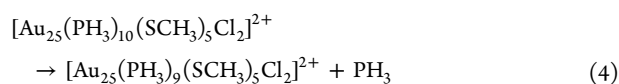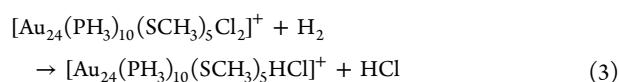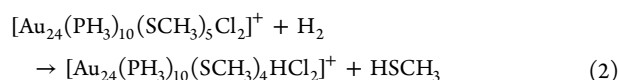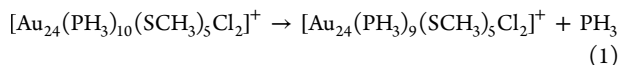
The reaction enthalpies for the full depassivation reactions (eqs 7 and 8) were also predicted.

$$[Au_{24}(PH_3)_{10}(SCH_3)_5Cl_2]^+ + \frac{7}{2}H_2$$
$$\rightarrow Au_{24}^+ + 5HSCH_3 + 10PH_3 + 2HCl \tag{7}$$

$$[Au_{25}(PH_3)_{10}(SCH_3)_5Cl_2]^{2+} + \frac{7}{2}H_2$$
$$\rightarrow Au_{25}^{2+} + 5HSCH_3 + 10PH_3 + 2HCl \tag{8}$$
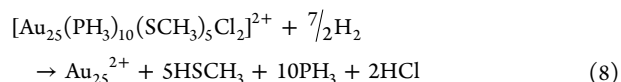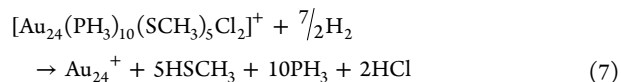
For the optimization of the fully depassivated clusters, we deleted all of the atoms except Au atoms from the optimized $[Au_{24}(PH_3)_{10}(SCH_3)_5Cl_2]^+$ and $[Au_{25}(PH_3)_{10}(SCH_3)_5Cl_2]^{2+}$, and local geometry optimization for the remaining pure Au_{24}^+ and Au_{25}^{2+} clusters was performed. The cluster structures obtained from the local geometry optimization calculations were compared to the cluster structures obtained from the AIMD simulations.

The initial aggregation reaction of the fully depassivated Au_{24}^+ and Au_{25}^{2+} clusters was investigated by considering Au migration reactions given in eqs 9–12, from which the Au dissociation energy and Au affinity for Au_{24}^+ and Au_{25}^{2+} were derived. Only surface Au atoms were considered for the addition and removal.

$$Au_{24}^+(\text{double-cage}) \rightarrow Au_{23}^+ + Au \tag{9}$$

$$Au_{24}^+(\text{double-cage}) + Au \rightarrow Au_{25}^+ \tag{10}$$

$$Au_{25}^{2+}(\text{close-packed}) \rightarrow Au_{24}^{2+} + Au \tag{11}$$

$$Au_{25}^+(\text{close-packed}) + Au \rightarrow Au_{26}^{2+} \tag{12}$$
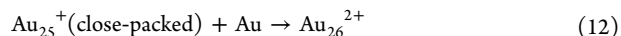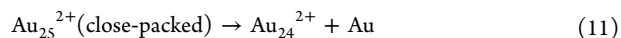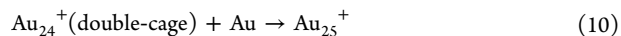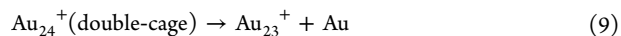
The potential energy surface for the CO_2 hydrogenation reaction leading to DME was predicted at the DFT level. CO_2 hydrogenation that involves one CO_2 molecule was first considered, for which we constructed possible intermediates for each elementary hydrogenation step $(+\frac{1}{2}H_2)$. The CO_2 hydrogenation that involves two CO_2 molecules and eventually leads to formation of a C_2 product (DME) was next considered by repeating the one-CO_2 reaction at a site adjacent to the existing (already considered) active site. Zero-point energy corrections were included in the reaction energies, and thus, the potential energy surfaces were constructed with reaction enthalpies at 0 K.

■ ASSOCIATED CONTENT

Ⓢ Supporting Information

The Supporting Information is available free of charge at https://pubs.acs.org/doi/10.1021/jacs.9b07761.

Supporting Figures S1–S15 and Tables S1 and S2 (PDF)

■ AUTHOR INFORMATION

Corresponding Authors

Mingyang Chen – *Center for Green Innovation, School of Materials Science and Engineering, University of Science and Technology Beijing, Beijing 100083, China; Beijing Computational Science Research Center, Beijing 100193, China;* ⓞ orcid.org/0000-0002-9866-8695; Email: mychen@ustb.edu.cn

Rui Si – *Shanghai Synchrotron Radiation Facility, Zhangjiang Laboratory, Shanghai 201204, China;* Email: sirui@sinap.ac.cn

Yan Zhu – *School of Chemistry and Chemical Engineering, Nanjing University, Nanjing 210093, China;* ⓞ orcid.org/0000-0002-5993-4110; Email: zhuyan@nju.edu.cn

Authors

Xiao Cai − *School of Chemistry and Chemical Engineering, Nanjing University, Nanjing 210093, China*

Weigang Hu − *School of Chemistry and Chemical Engineering, Nanjing University, Nanjing 210093, China*

Shun Xu − *School of Chemistry and Chemical Engineering, Nanjing University, Nanjing 210093, China*

Dan Yang − *School of Chemistry and Chemical Engineering, Nanjing University, Nanjing 210093, China*

Miao Shu − *Shanghai Synchrotron Radiation Facility, Zhangjiang Laboratory, Shanghai 201204, China*

Weiping Ding − *School of Chemistry and Chemical Engineering, Nanjing University, Nanjing 210093, China;* ⓞ orcid.org/0000-0002-8034-5740

Complete contact information is available at:
https://pubs.acs.org/10.1021/jacs.9b07761

Notes

The authors declare no competing financial interest.

■ REFERENCES

(1) Fu, Q.; Bao, X. Surface chemistry and catalysis confined under two-dimensional materials. *Chem. Soc. Rev.* **2017**, *46*, 1842−1874.

(2) Liu, P.; Qin, R.; Fu, G.; Zheng, N. Surface Coordination Chemistry of Metal Nanomaterials. *J. Am. Chem. Soc.* **2017**, *139*, 2122−2131.

(3) Somorjai, G. A.; Li, Y. *Introduction to Surface Chemistry and Catalysis*; John Wiley & Sons: Hoboken, NJ, 2010.

(4) Somorjai, G. A.; Park, J. Y. Molecular Factors of Catalytic Selectivity. *Angew. Chem., Int. Ed.* **2008**, *47*, 9212−9228.

(5) Wu, Y.; Wang, D.; Li, Y. Nanocrystals from solutions: catalysts. *Chem. Soc. Rev.* **2014**, *43*, 2112−2124.

(6) Zhang, L.; Roling, L. T.; Wang, X.; Vara, M.; Chi, M.; Liu, J.; Choi, S.; Park, J.; Herron, J. A.; Xie, Z.; Mavrikakis, M.; Xia, Y. Platinum-based nanocages with subnanometer-thick walls and well-defined, controllable facets. *Science* **2015**, *349*, 412−416.

(7) Crampton, A. S.; Rötzer, M. D.; Ridge, C. J.; Schweinberger, F. F.; Heiz, U.; Yoon, B.; Landman, U. Structure sensitivity in the nonscalable regime explored via catalysed ethylene hydrogenation on supported platinum nanoclusters. *Nat. Commun.* **2016**, *7*, 10389.

(8) Lang, S. M.; Fleischer, I.; Bernhardt, T. M.; Barnett, R. N.; Landman, U. Low-Temperature CO Oxidation Catalyzed by Free Palladium Clusters: Similarities and Differences to Pd Surfaces and Supported Particles. *ACS Catal.* **2015**, *5*, 2275−2289.

(9) Zhai, H.; Alexandrova, A. N. Local Fluxionality of Surface-Deposited Cluster Catalysts: The Case of Pt7 on Al2O3. *J. Phys. Chem. Lett.* **2018**, *9*, 1696−1702.

(10) Ha, M. A.; Baxter, E. T.; Cass, A. C.; Anderson, S. L.; Alexandrova, A. N. Boron Switch for Selectivity of Catalytic Dehydrogenation on Size-Selected Pt Clusters on Al2O3. *J. Am. Chem. Soc.* **2017**, *139*, 11568−11575.

(11) Jadzinsky, P. D.; Calero, G.; Ackerson, C. J.; Bushnell, D. A.; Kornberg, R. D. Structure of a Thiol Monolayer-Protected Gold Nanoparticle at 1.1 Å Resolution. *Science* **2007**, *318*, 430−433.

(12) Desireddy, A.; Conn, B. E.; Guo, J.; Yoon, B.; Barnett, R. N.; Monahan, B. M.; Kirschbaum, K.; Griffith, W. P.; Whetten, R. L.; Landman, U.; Bigioni, T. P. Ultrastable silver nanoparticles. *Nature* **2013**, *501*, 399−402.

(13) Azubel, M.; Koivisto, J.; Malola, S.; Bushnell, D.; Hura, G. L.; Koh, A. L.; Tsunoyama, H.; Tsukuda, T.; Pettersson, M.; Häkkinen, H.; Kornberg, R. D. Electron microscopy of gold nanoparticles at atomic resolution. *Science* **2014**, *345*, 909−912.

(14) Jin, R.; Zeng, C.; Zhou, M.; Chen, Y. Atomically Precise Colloidal Metal Nanoclusters and Nanoparticles: Fundamentals and Opportunities. *Chem. Rev.* **2016**, *116*, 10346−10413.

(15) Gan, Z.; Lin, Y.; Luo, L.; Han, G.; Liu, W.; Liu, Z.; Yao, C.; Weng, L.; Liao, L.; Chen, J.; Liu, X.; Luo, Y.; Wang, C.; Wei, S.; Wu, Z. Fluorescent Gold Nanoclusters with Interlocked Staples and a Fully Thiolate-Bound Kernel. *Angew. Chem., Int. Ed.* **2016**, *55*, 11567−11571.

(16) Yuan, S.; Xu, C.; Li, J.; Wang, Q. Ligand-Protected "Golden Fullerene": the Dipyridylamido Au32^8+ Nanocluster. *Angew. Chem., Int. Ed.* **2019**, *58*, 5906−5909.

(17) Luo, Z.; Nachammai, V.; Zhang, B.; Yan, N.; Leong, D. T.; Jiang, D.; Xie, J. Toward Understanding the Growth Mechanism: Tracing All Stable Intermediate Species from Reduction of Au(I)−thiolate Complexes to Evolution of Au25 Nanoclusters. *J. Am. Chem. Soc.* **2014**, *136*, 10577−10580.

(18) Jin, S.; Wang, S.; Song, Y.; Zhou, M.; Zhong, J.; Zhang, J.; Xia, A.; Pei, Y.; Chen, M.; Li, P.; Zhu, M. Crystal Structure and Optical Properties of the [Ag62S12(SBut)32]^2+ Nanocluster with a Complete Face-Centered Cubic Kernel. *J. Am. Chem. Soc.* **2014**, *136*, 15559−15565.

(19) Tyo, E. C.; Vajda, S. Catalysis by clusters with precise numbers of atoms. *Nat. Nanotechnol.* **2015**, *10*, 577−588.

(20) Yamazoe, S.; Koyasu, K.; Tsukuda, T. Nonscalable Oxidation Catalysis of Gold Clusters. *Acc. Chem. Res.* **2014**, *47*, 816−824.

(21) Li, G.; Jin, R. Atomically Precise Gold Nanoclusters as New Model Catalysts. *Acc. Chem. Res.* **2013**, *46*, 1749−1758.

(22) Shoshani, M. M.; Johnson, S. A. Cooperative carbon-atom abstraction from alkenes in the core of a pentanuclear nickel cluster. *Nat. Chem.* **2017**, *9*, 1282−1285.

(23) Qian, H.; Jiang, D.; Li, G.; Gayathri, C.; Das, A.; Gil, R. R.; Jin, R. Monoplatinum Doping of Gold Nanoclusters and Catalytic Application. *J. Am. Chem. Soc.* **2012**, *134*, 16159−16162.

(24) Xie, S.; Tsunoyama, H.; Kurashige, W.; Negishi, Y.; Tsukuda, T. Enhancement in Aerobic Alcohol Oxidation Catalysis of Au25 Clusters by Single Pd Atom Doping. *ACS Catal.* **2012**, *2*, 1519−1523.

(25) Liu, Y.; Chai, X.; Cai, X.; Chen, M.; Jin, R.; Ding, W.; Zhu, Y. Central Doping of a Foreign Atom into the Silver Cluster for Catalytic Conversion of CO2 toward C-C Bond Formation. *Angew. Chem., Int. Ed.* **2018**, *57*, 9775−9779.

(26) Kwak, K.; Choi, W.; Tang, Q.; Kim, M.; Lee, Y.; Jiang, D.; Lee, D. A molecule-like PtAu24(SC6H13)18 nanocluster as an electrocatalyst for hydrogen production. *Nat. Commun.* **2017**, *8*, 14723.

(27) Cai, X.; Saranya, G.; Shen, K.; Chen, M.; Si, R.; Ding, W.; Zhu, Y. Reversible Switching of Catalytic Activity by Shuttling an Atom into and out of Au Nanoclusters. *Angew. Chem., Int. Ed.* **2019**, *58*, 9964−9968.

(28) Yang, X.; Kattel, S.; Senanayake, S. D.; Boscoboinik, J. A.; Nie, X.; Graciani, J.; Rodriguez, J. A.; Liu, P.; Stacchiola, D. J.; Chen, J. G. Low Pressure CO2 Hydrogenation to Methanol over Gold Nanoparticles Activated on a CeOx/TiO2 Interface. *J. Am. Chem. Soc.* **2015**, *137*, 10104−10107.

(29) Rezayee, N. M.; Huff, C. A.; Sanford, M. S.; Amine, T. Ruthenium-Catalyzed Hydrogenation of CO2 to Methanol. *J. Am. Chem. Soc.* **2015**, *137*, 1028−1031.

(30) Bai, S.; Shao, Q.; Wang, P. T.; Dai, Q.; Wang, X.; Huang, X. Highly Active and Selective Hydrogenation of CO2 to Ethanol by Ordered Pd-Cu Nanoparticles. *J. Am. Chem. Soc.* **2017**, *139*, 6827−6830.

(31) Wang, L.; Wang, L.; Zhang, J.; Liu, X.; Wang, H.; Zhang, W.; Yang, Q.; Ma, J.; Dong, X.; Yoo, S. J.; Kim, J.; Meng, X.; Xiao, F. Selective Hydrogenation of CO2 to Ethanol over Cobalt Catalysts. *Angew. Chem., Int. Ed.* **2018**, *57*, 6104−6108.

(32) Liu, Q.; Yang, X.; Li, L.; Miao, S.; Li, Y.; Li, Y.; Wang, X.; Huang, Y.; Zhang, T. Direct catalytic hydrogenation of CO2 to formate over a Schiff-base-mediated gold nanocatalyst. *Nat. Commun.* **2017**, *8*, 1407.

(33) He, Z.; Cui, M.; Qian, Q.; Zhang, J.; Liu, H.; Han, B. Synthesis of liquid fuel via direct hydrogenation of CO_2. *Proc. Natl. Acad. Sci. U. S. A.* **2019**, *116*, 12654−12659.

(34) An, B.; Zeng, L.; Jia, M.; Li, Z.; Lin, Z.; Song, Y.; Zhou, Y.; Cheng, J.; Wang, C.; Lin, W. Molecular Iridium Complexes in Metal-Organic Frameworks Catalyze CO_2 Hydrogenation via Concerted Proton and Hydride Transfer. *J. Am. Chem. Soc.* **2017**, *139*, 17747−17750.

(35) Kar, S.; Sen, R.; Goeppert, A.; Prakash, G. K. S. Integrative CO_2 Capture and Hydrogenation to Methanol with Reusable Catalyst and Amine: Toward a Carbon Neutral Methanol Economy. *J. Am. Chem. Soc.* **2018**, *140*, 1580−1583.

(36) Das, A.; Li, T.; Nobusada, K.; Zeng, Q.; Rosi, N. L.; Jin, R. Total Structure and Optical Properties of a Phosphine/Thiolate-Protected Au_{24} Nanocluster. *J. Am. Chem. Soc.* **2012**, *134*, 20286−20289.

(37) Jin, R.; Liu, C.; Zhao, S.; Das, A.; Xing, H.; Gayathri, C.; Xing, Y.; Rosi, N. L.; Gil, R. R.; Jin, R. Tri-icosahedral Gold Nanocluster $[Au_{37}(PPh_3)_{10}(SC_2H_4Ph)_{10}X_2]^+$: Linear Assembly of Icosahedral Building Blocks. *ACS Nano* **2015**, *9*, 8530−8536.

(38) Qian, H.; Eckenhoff, W. T.; Zhu, Y.; Pintauer, T.; Jin, R. Total Structure Determination of Thiolate-Protected Au_{38} Nanoparticles. *J. Am. Chem. Soc.* **2010**, *132*, 8280−8281.

(39) Guo, L.; Du, P.; Fu, X.; Ma, C.; Zeng, J.; Si, R.; Huang, Y.; Jia, C.; Zhang, Y.; Yan, C. Contributions of distinct gold species to catalytic reactivity for carbon monoxide oxidation. *Nat. Commun.* **2016**, *7*, 13481.

(40) Zhang, P. X-ray Spectroscopy of Gold−Thiolate Nanoclusters. *J. Phys. Chem. C* **2014**, *118*, 25291−25299.

(41) Yamazoe, S.; Takano, S.; Kurashige, W.; Yokoyama, T.; Nitta, K.; Negishi, Y.; Tsukuda, T. Hierarchy of bond stiffnesses within icosahedral-based gold clusters protected by thiolates. *Nat. Commun.* **2016**, *7*, 10414.

(42) Tong, P.; Xie, W.; Yang, D.; Wang, B.; Ji, X.; Li, J.; Qu, J. Structural characterization and proton reduction electrocatalysis of thiolate-bridged bimetallic (CoCo and CoFe) complexes. *Dalton Trans.* **2016**, *45*, 18559−18565.

(43) Dubis, E. N.; Dubis, A. T.; Morzycki, J. W. Comparative analysis of plant cuticular waxes using HATR FT-IR reflection technique. *J. Mol. Struct.* **1999**, *511−512*, 173−179.

(44) Hsu, W. H.; Shau, M. D. The properties of epoxy−imide resin cured by cyclic phosphine oxide diacid. *J. Appl. Polym. Sci.* **1996**, *62*, 427−433.

(45) Maghsoodlou, M. T.; Hazeri, N.; Khorassani, S. M. H.; Nassiri, M.; Marandi, G.; Afshari, G.; Niroumand, U. An efficient synthesis of stable sulfur-containing phosphoranes derived from 2-mercapto-1-methylimidazole and 2-thiazoline-2-thiol. *J. Sulfur Chem.* **2005**, *26*, 261−265.

(46) Wang, J.; Wang, G.; Zhao, J. Density-Functional Study of Au_n (n = 2−20) Clusters: Lowest-Energy Structures and Electronic Properties. *Phys. Rev. B: Condens. Matter Mater. Phys.* **2002**, *66*, No. 035418.

(47) Tian, D.; Zhang, H.; Zhao, J. Structure and structural evolution of Ag_n (n = 3−22) clusters using a genetic algorithm and density functional theory method. *Solid State Commun.* **2007**, *144*, 174−179.

(48) Li, J.; Li, X.; Zhai, H.; Wang, L. Au_{20}: A Tetrahedral Cluster. *Science* **2003**, *299*, 864−867.

(49) Gruene, P.; Rayner, D. M.; Redlich, B.; van der Meer, A. F. G.; Lyon, J. T.; Meijer, G.; Fielicke, A. Structures of Neutral Au_7, Au_{19}, and Au_{20} Clusters in the Gas Phase. *Science* **2008**, *321*, 674−676.

(50) Schooss, D.; Weis, P.; Hampe, O.; Kappes, M. M. Determining the size-dependent structure of ligand-free gold-cluster ions. *Philos. Trans. R. Soc., A* **2010**, *368*, 1211−1243.

(51) Bulusu, S.; Li, X.; Wang, L.; Zeng, X. Structural Transitions from Pyramidal to Fused Planar to Tubular to Core/Shell Compact in Gold Clusters: Au_n^- (n = 21−25). *J. Phys. Chem. C* **2007**, *111*, 4190−4198.

(52) Bulusu, S.; Li, X.; Wang, L.; Zeng, X. Evidence of hollow golden cages. *Proc. Natl. Acad. Sci. U. S. A.* **2006**, *103*, 8326−8330.

(53) Shao, N.; Huang, W.; Mei, W.; Wang, L.; Wu, Q.; Zeng, X. Structural Evolution of Medium-Sized Gold Clusters Au_n^- (n = 36, 37, 38): Appearance of Bulk-like Face Centered Cubic Fragment. *J. Phys. Chem. C* **2014**, *118*, 6887−6892.

(54) Pande, S.; Huang, W.; Shao, N.; Wang, L.; Khetrapal, N.; Mei, W.; Jian, T.; Wang, L.; Zeng, X. Structural Evolution of Core−Shell Gold Nanoclusters: Au_n^- (n = 42−50). *ACS Nano* **2016**, *10*, 10013−10022.

(55) Wood, B. R.; Reimer, J. A.; Bell, A. T.; Janicke, M. T.; Ott, K. C. Methanol formation on Fe/Al-MFI via the oxidation of methane by nitrous oxide. *J. Catal.* **2004**, *225*, 300−306.

(56) Kéranguéven, G.; Coutanceau, C.; Sibert, E.; Hahn, F.; Léger, J. M.; Lamy, C. Mechanism of di(methyl)ether (DME) electrooxidation at platinum electrodes in acid medium. *J. Appl. Electrochem.* **2006**, *36*, 441−448.

(57) Zhang, W.; Wang, L.; Liu, H.; Hao, Y.; Li, H.; Khan, M. U.; Zeng, J. Integration of Quantum Confinement and Alloy Effect to Modulate Electronic Properties of RhW Nanocrystals for Improved Catalytic Performance toward CO_2 Hydrogenation. *Nano Lett.* **2017**, *17*, 788−793.

(58) Wang, L.; Zhang, W.; Zheng, X.; Chen, Y.; Wu, W.; Qiu, J.; Zhao, X.; Zhao, X.; Dai, Y.; Zeng, J. Incorporating nitrogen atoms into cobalt nanosheets as a strategy to boost catalytic activity toward CO_2 hydrogenation. *Nat. Energy* **2017**, *2*, 869−876.

(59) Ma, M.; Zhan, E.; Huang, X.; Ta, N.; Xiong, Z.; Bai, L.; Shen, W. Carbonylation of dimethyl ether over Co-HMOR. *Catal. Sci. Technol.* **2018**, *8*, 2124−2130.

(60) Kumar, P.; Shrivastava, B.; Pandeya, S. N.; Tripathi, L.; Stables, J. P. Design, synthesis, and anticonvulsant evaluation of some novel 1, 3 benzothiazol-2-yl hydrazones/acetohydrazones. *Med. Chem. Res.* **2012**, *21*, 2428−2442.

(61) Schneider, J.; Erdelen, C.; Ringsdorf, H.; Rabolt, J. F. Structural studies of polymers with hydrophilic spacer groups. 2. Infrared spectroscopy of Langmuir-Blodgett multilayers of polymers with fluorocarbon side chains at ambient and elevated temperatures. *Macromolecules* **1989**, *22*, 3475−3480.

(62) Chuang, C.; Wu, W.; Huang, M.; Huang, I.; Lin, J. FTIR study of adsorption and reactions of methyl formate on powdered TiO_2. *J. Catal.* **1999**, *185*, 423−434.

(63) Bezrodna, T.; Puchkovska, G.; Shymanovska, V.; Baran, J.; Ratajczak, H. IR-analysis of h-bonded H_2O on the pure TiO_2 surface. *J. Mol. Struct.* **2004**, *700*, 175−181.

(64) Wu, Z.; Jiang, D.; Mann, A. K. P.; Mullins, D. R.; Qiao, Z.; Allard, L. F.; Zeng, C.; Jin, R.; Overbury, S. H. Thiolate Ligands as a Double-Edged Sword for CO Oxidation on CeO_2 Supported $Au_{25}(SCH_2CH_2Ph)_{18}$ Nanoclusters. *J. Am. Chem. Soc.* **2014**, *136*, 6111−6122.

(65) Kattel, S.; Ramírez, P. J.; Chen, J. G.; Rodriguez, J. A.; Liu, P. Active sites for CO_2 hydrogenation to methanol on Cu/ZnO catalysts. *Science* **2017**, *355*, 1296−1299.

(66) Azizi, Z.; Rezaeimanesh, M.; Tohidian, T.; Rahimpour, M. R. Dimethyl ether: A review of technologies and production challenges. *Chem. Eng. Process.* **2014**, *82*, 150−172.

(67) Yu, H.; Wei, X.; Li, J.; Gu, S.; Zhang, S.; Wang, L.; Ma, J.; Li, L.; Gao, Q.; Si, R.; Sun, F.; Wang, Y.; Song, F.; Xu, H.; Yu, X.; Zou, Y.; Wang, J.; Jiang, Z.; Huang, Y. The XAFS beamline of SSRF. *Nucl. Sci. Technol.* **2015**, *26*, No. 050102.

(68) Becke, A. D. Density-functional thermochemistry. III. The role of exact exchange. *J. Chem. Phys.* **1993**, *98*, 5648−5652.

(69) Perdew, J. P.; Burke, K.; Ernzerhof, M. Generalized Gradient Approximation Made Simple. *Phys. Rev. Lett.* **1996**, *77*, 3865−3868.

(70) Frisch, M. J.; Trucks, G. W.; Schlegel, H. B.; Scuseria, G. E.; Robb, M. A.; Cheeseman, J. R.; Scalmani, G.; Barone, V.; Mennucci, B.; Petersson, G. A.; Nakatsuji, H.; Caricato, M.; Li, X.; Hratchian, H. P.; Izmaylov, A. F.; Bloino, J.; Zheng, G.; Sonnenberg, J. L.; Hada, M.; Ehara, M.; Toyota, K.; Fukuda, R.; Hasegawa, J.; Ishida, M.; Nakajima, T.; Honda, Y.; Kitao, O.; Nakai, H.; Vreven, T.; Montgomery, J. A., Jr.; Peralta, J. E.; Ogliaro, F.; Bearpark, M.; Heyd, J. J.; Brothers, E.; Kudin, K. N.; Staroverov, V. N.; Kobayashi,

R.; Normand, J.; Raghavachari, K.; Rendell, A.; Burant, J. C.; Iyengar, S. S.; Tomasi, J.; Cossi, M.; Rega, N.; Millam, N. J.; Klene, M.; Knox, J. E.; Cross, J. B.; Bakken, V.; Adamo, C.; Jaramillo, J.; Gomperts, R.; Stratmann, R. E.; Yazyev, O.; Austin, A. J.; Cammi, R.; Pomelli, C.; Ochterski, J. W.; Martin, R. L.; Morokuma, K.; Zakrzewski, V. G.; Voth, G. A.; Salvador, P.; Dannenberg, J. J.; Dapprich, S.; Daniels, A. D.; Farkas, Ö.; Foresman, J. B.; Ortiz, J. V.; Cioslowski, J.; Fox, D. J. *Gaussian 09*, revision B.01; Gaussian, Inc.: Wallingford, CT, 2009.

(71) Marx, D.; Hutter, J. *Ab Initio Molecular Dynamics: Basic Theory and Advanced Methods*, 1st ed.; Cambridge University Press: Cambridge, U.K., 2009.

(72) Nosé, S. A unified formulation of the constant temperature molecular dynamics methods. *J. Chem. Phys.* **1984**, *81*, 511−519.

(73) Hoover, W. G. Canonical dynamics: Equilibrium phase-space distributions. *Phys. Rev. A: At., Mol., Opt. Phys.* **1985**, *31*, 1695−1697.

(74) Lippert, G.; Hutter, J.; Parrinello, M. The Gaussian and augmented-plane-wave density functional method for ab initio molecular dynamics simulations. *Theor. Chem. Acc.* **1999**, *103*, 124−140.

(75) VandeVondele, J.; Krack, M.; Mohamed, F.; Parrinello, M.; Chassaing, T.; Hutter, J. Quickstep: Fast and accurate density functional calculations using a mixed gaussian and plane waves approach. *Comput. Phys. Commun.* **2005**, *167*, 103−128.

(76) VandeVondele, J.; Hutter, J. Gaussian Basis Sets for Accurate Calculations on Molecular Systems in Gas and Condensed Phases. *J. Chem. Phys.* **2007**, *127*, 114105.

(77) Kendall, R. A.; Dunning, T. H.; Harrison, R. J. Electron-affinities of the 1st-row atoms revisited-systematic basis-sets and wave-functions. *J. Chem. Phys.* **1992**, *96*, 6796−6806.

(78) Peterson, K. A. Systematically convergent basis sets with relativistic pseudopotentials. I. Correlation consistent basis sets for the post-d group 13−15 elements. *J. Chem. Phys.* **2003**, *119*, 11099−11112.

(79) Peterson, K. A.; Figgen, D.; Goll, E.; Stoll, H.; Dolg, M. Systematically convergent basis sets with relativistic pseudopotentials. II. Small-core pseudopotentials and correlation consistent basis sets for the post-d group 16−18 elements. *J. Chem. Phys.* **2003**, *119*, 11113−11123.